



Polymeric interfacial engineering approach to perovskite-functionalized organic transistor-type gas sensors

Duho Jang^{a,1}, Haedam Jin^{b,1}, Min Kim^{c,*}, Yeong Don Park^{a,*}

^a Department of Energy and Chemical Engineering, Incheon National University, Incheon 22012, Republic of Korea

^b Graduate School of Integrated Energy-AI, Jeonbuk National University, Jeonju 54896, Republic of Korea

^c School of Chemical Engineering, Clean Energy Research Center, Jeonbuk National University, Jeonju 54896, Republic of Korea

ARTICLE INFO

Keywords:

NO₂ gas sensors
Inorganic-organic hybrid
P3HT
Perovskite
Nanocrystals

ABSTRACT

Organic semiconductors (OSCs) are promising sensing materials for printed organic gas sensors. Although OSCs show promise since they are mechanically flexible, cost-effective, and lightweight, they still face challenges related to low sensitivity and poor stability under ambient conditions; their development therefore lags that of inorganic-based gas sensors. Functional nanomaterials can be incorporated into organic semiconductors to complement the gas sensitivity and stability. Herein, we describe the fabrication of novel organic-inorganic hybrid gas sensors via the blending of perovskite nanocrystals and conductive polymer. We introduced a perovskite-structured material, CsPbBr₃, into a conductive polymer matrix, which substantially improved its gas-sensing performance while maintaining its high responsivity and response rates. To further improve the adsorption of target gas molecules, we modified the surface of the perovskite using a zwitterionic polymer subjected to a hydration treatment. The results demonstrate that the amide group of the encapsulation polymer exhibits high affinity toward NO₂ gas molecules and that this affinity becomes more pronounced upon hydration of the polymer. We also demonstrate the perovskite materials in the semiconducting polymer layer can protect the polymer thin film against oxidation during prolonged storage under ambient conditions because of the perovskite crystals' ability to adsorb oxidizing molecules.

1. Introduction

Recently, with the rapid expansion of industrialization, the invention of smart gas sensors for the early detection of air pollutants such as nitrogen compounds, carbides, sulfides, and volatile organic compounds has attracted enormous research attention for ensuring human respiratory health[1,2]. Among hazardous gases, NO₂, which is typically released from the combustion of fossil fuels, can lead to serious respiratory diseases in humans, including pulmonary edema, bronchitis, and asthma. The Health and Safety Rule Alarm has mentioned that the human body should not be exposed for longer than 8 h in an environment of 3 ppm NO₂[3–5]. Therefore, NO₂ should be monitored using ultrasensitive, highly selective, and long-term-stable gas sensors, for which different organic and inorganic materials have been utilized.

Gas-sensing devices include gas chromatography sensors, electrochemical sensors, optical sensors, and resistive and capacitive sensors. Gas chromatography sensors exhibit high performance but a slow

response and high-power consumption; in addition, gas chromatography is time-consuming and requires expensive equipment[6]. Electrochemical sensors require a solution-based device system that dissolves the target gas, which adds complexity to the system[7]. Optical gas sensors are difficult to miniaturize and take time transducing chemical to optical information[8]. Because of these drawbacks, researchers have focused on semiconductor-based resistive and capacitive sensor devices. Recently, conductive polymers have attracted a lot of attention due to their wide variety of materials, good flexibility, good compatibility with large area fabricating methods, and light weight [9,10]. In addition, they can also be manufactured into portable gas sensors by a simple solution process[11]. Especially, organic field effect transistor (OFET)-based gas sensors are attracting attention because they can be potentially applied to signal amplifiers.

The gas detection function of OFET devices is closely related to the intermolecular interaction between gas analyte and the organic semiconductor, which operates via a charge transfer or electronic doping

* Corresponding authors.

E-mail addresses: minkim@jnu.ac.kr (M. Kim), ypark@inu.ac.kr (Y. Don Park).

¹ These authors contributed equally to the work.

mechanism at the contact area of analytes on semiconductor layers[12]. In the thin-film geometry of an OFET, the charge carriers in the conduction channels are strongly modulated under an applied gate bias. However, a charge conduction channel is formed within a thickness of a few nanometers at the dielectric interface, which makes interaction of the analyte molecules with the conductive layer difficult[13,14]. Researchers have therefore attempted to improve the sensing performance by enhancing gas penetration into the semiconductor layer, such as by adjusting the film thickness to be ultrathin, modulating the nanostructure of the organic semiconductors, and constructing nanoporous structures with sacrificial components [15–17]. Several fabrication methods have been developed to obtain nanoporous morphologies exhibiting high gas-sensing properties. These include the shearing-assisted phase separation method, which achieves a sensitivity of 7 % ppm⁻¹ to NH₃; the vacuum free-drying method, with a sensitivity of 340 % ppm⁻¹ to NH₃; the P3HT:SEBS polymer blend method, achieving a sensitivity of 467 % ppm⁻¹ to NO₂; and the meniscus-guided printing method, with a limit of detection around 1 ppb [18–21]. However, solution-based processing often introduces complexity in film formation and leads to unstable device operations [22].

The gas-adsorbing properties of materials are strongly influenced by the materials' relative surface area and ability to interact with gas molecules. Nanostructured materials with functionally modified surfaces have been developed to achieve adequate gas-adsorption performance. Various inorganic functional materials, including porous inorganic materials, carbon allotropes, and metal oxides, have been chosen to enhance the gas sensing sensitivity of OFET-based sensors [23–25]. However, these materials are prepared via complex multistep processes and their surface tunability is limited. Recently, metal halide perovskite-type materials have attracted intensive attention due to their wide chemical tunability, unique optoelectronic properties, and ease of preparation as nanoparticles[26–28]. Not only have halide perovskites demonstrated excellent photovoltaic performance, but perovskite materials, tailored into nanocrystals (NCs), have been found to exhibit unique nanocrystalline properties, with a large surface-to-volume ratio and various surface chemistries[29]. The surface chemical modification of perovskites, which is possible through modification of the perovskite composition and the use of surface-coordinating ligand molecules, offers a rich opportunity for achieving strong interactions with gas molecules. Surface-engineered perovskite NCs can thus be used in OTFT gas-sensing devices because of their strong interaction with gases[30–32]. However, literature on the hybridization of perovskite derivative nanomaterials with organic semiconductor-based gas sensor devices remains scarce despite the strong reactivity of such nanomaterials toward molecular substances.

In the present study, we manufactured a greatly sensitive OFET-based gas sensor by using perovskite NCs as the gas-sensitive element and a conductive polymer, poly(3-hexylthiophene) (P3HT), as the charge transport host in the semiconducting layer of an OFET. We modified the surface chemical properties of the perovskite NCs via a ligand-exchange treatment, resulting in encapsulation of the NCs by a zwitterionic polymer that strongly interacts not only with the perovskite NCs' surface but also with target gas molecules. In addition, we used hydrated perovskite NCs to maximize their NO₂ capturing ability via water–NO₂ interactions. This hybridization of polymer-modified perovskite NCs provides the semiconductor polymer matrix with optimum structuring at various levels of structural organization, and this structuring leads to the fabrication of a semiconducting polymer with effective and ultrasensitive gas-sensing properties for selective detection of target gas molecules. The developed OFET gas sensor was further investigated in terms of device stability under ambient storage for 21 days.

2. Results and discussion

We prepared CsPbBr₃ perovskite NCs using a modified hot-injection

technique[33,34]. The size of the CsPbBr₃ NCs ranged from 10 to 20 nm; such NCs have a high surface-to-volume ratio of $\sim 3 \times 10^8 \text{ m}^{-1}$, providing a high density of gas adsorption sites. In the present study, to improve the gas-adsorbing ability of the CsPbBr₃ perovskite NCs, we modified their surface with a zwitterionic polymer containing both amino and carboxylate functional groups. These groups strongly interact with components of the perovskite NCs' surface, leading to robust attachment, and strongly adsorb oxidizing gases via hydrogen-bonding forces. The zwitterionic polymer used for ligand exchange in a solution state was poly(carboxybetaine acrylamide) (PCA). The polymer solution was mixed with the CsPbBr₃ NC solution to ensure ligand exchange from the oleic acid to the PCA, forming PCA-exchanged CsPbBr₃ nanocrystals (PCA-NCs). We further prepared hydrated PCA by adding water to the polymer solution and applied it to the perovskite NCs' surface to obtain hydrated-PCA CsPbBr₃ perovskite nanocrystals (PCA-w-NCs) (Fig. 1a). The water molecules are strongly bound to the PCA molecules via hydrogen bonding.

The perovskite NCs are aggregated and encapsulated by the PCA, forming a sheath layer of PCA. The individual CsPbBr₃ NCs are chamfered but retain their cubic perovskite structure. With PCA encapsulation, the perovskite NCs form 100 nm agglomerations (Fig. 1b). With the addition of water molecules, the chamfered CsPbBr₃ NCs become smaller and rounder. A Transmission electron microscope (TEM) image of a single perovskite NC indicates a size of approximately 5–15 nm. The supra-particles form round agglomerates approximately 100 nm in diameter. The NCs are encapsulated with PCA, forming a sheath layer with 10–20 nm thickness.

The X-ray diffraction (XRD) profiles of the pristine perovskite NCs, PCA-NCs, and PCA-w-NCs exhibit identical cubic perovskite phases, as confirmed by the reference pattern for CsPbBr₃ perovskite with Pnma space symmetry (Fig. 1c) [35]. Even in the case of water treatment, the cubic perovskite structure was not deteriorated but well maintained. Therefore, we rule out changes in the crystalline properties of the perovskite and focus on the intermolecular interaction between PCA and the perovskite NCs.

To confirm the attachment of the polymer to the nanoparticles, we characterized the samples with the Fourier transform infrared (FT-IR) spectroscopy (Fig. 1d). The transmission spectra of the pristine PCA polymer show characteristic peaks at 1662 cm⁻¹ originating from the C = O stretching mode of methacrylate and peptide groups; this peak is only obtained in the spectra of the PCA-NCs and PCA-w-NCs, which indicates the successful exchange of PCA for oleic acid (OA) capping ligands on the perovskite NCs' surface [36,37]. The FT-IR spectra of the pristine perovskite NCs' with OA and oleylamine (OAm) capping ligands show prominent alkyl stretching peaks at 2800 and 2980 cm⁻¹, which are not discernable in the spectra of the PCA-NCs and PCA-w-NCs. The FT-IR spectra of the PCA-NCs show peaks identical to those in the spectrum of the pristine PCA polymer. The FT-IR peaks at 3300 cm⁻¹ originating from ammonium groups are marked by blue bands in Fig. 1d. In addition, the broad peak in the range of 2350–3300 cm⁻¹ in the spectra of the PCA-w-NCs is strongly enhanced because of the overlap of the OH stretching mode arising from water molecules intercalated into the PCA polymer chains (Fig. 1e) [38].

We further used X-ray photoelectron spectroscopy (XPS) to investigate the chemical encapsulation of the perovskite NCs with the PCA polymer. The N1s and O1s signals detected in the XPS analysis of the CsPbBr₃ NCs can be attributed to the oleic acid and oleylamine used as long-chain ligands during the synthesis of the NCs [39,40]. The C 1 s, N 1 s, and O 1 s spectra show that the OA/OAm surface ligands were successfully replaced with PCA. The singular peak in the C 1 s spectra of the pristine perovskite NCs shifts to higher binding energies and becomes a triple peak associated with O–C = O and C–N in the C 1 s spectrum of the nanoparticles encapsulated by PCA (Fig. 2a). A comparison of the atomic carbon content among the samples shows that the OA/OAm ligands were successfully exchanged for PCA polymers (Fig. 2d). The N 1 s peaks from the PCA-NCs become more intense

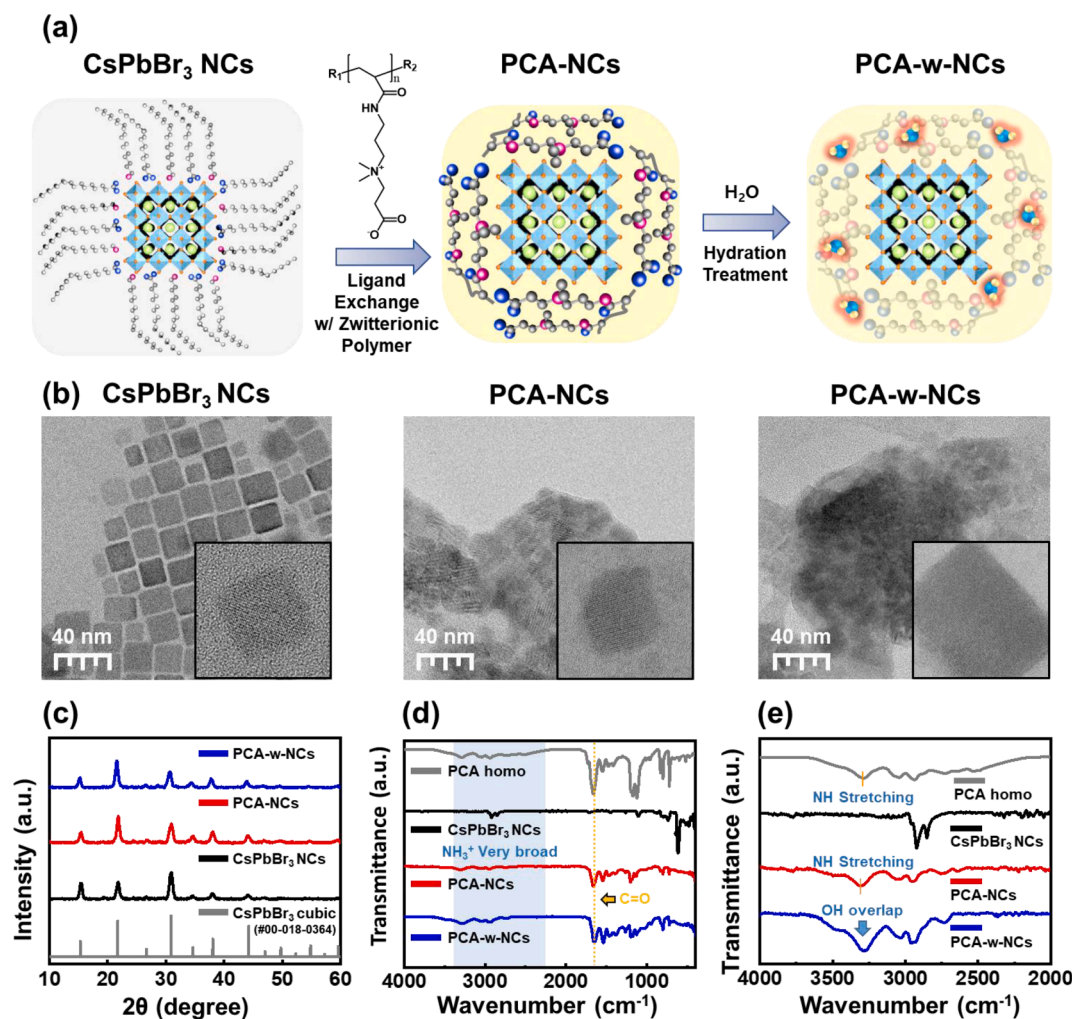


Fig. 1. (a) Schematic of a CsPbBr₃ perovskite-structured nanocrystal (NC) subjected to polymeric ligand exchange. (b) TEM images of the CsPbBr₃ perovskite NCs before and after their modification via polymeric ligand exchange and water-saturated polymeric ligand exchange. (c) XRD patterns of the pristine CsPbBr₃ perovskite NCs before and after their modification via polymeric ligand exchange and water-saturated polymeric ligand exchange. (d) FT-IR spectra of the pristine CsPbBr₃ perovskite NCs before and after their modification via polymeric ligand exchange and water-saturated polymeric ligand exchange. (e) Magnified FT-IR spectra of the CsPbBr₃ NCs before and after their encapsulation with PCA and PCA-w.

because of the large amount of N in the PCA polymer (Fig. 2b). The further treatment of the PCA polymer with water also modified the surface state of the perovskite NCs, whereas the C 1 s and N 1 s spectra of the PCA-w-NCs are analogous to those of the PCA-NCs.

The O 1 s spectrum of the perovskite NCs originates from the OA, whereas the O 1 s spectrum of the PCA-NCs shows a peak shift to a lower binding energy because of the carboxylic acid and the spectrum of the hydrated PCA-w-perovskite NCs shows an additional peak at a higher binding energy because of the water molecules attached to the PCA polymer (Fig. 2c). The N and O atomic compositions reflect the surface states of the PCA-NCs and PCA-w-NCs (Fig. 2e and 2f). When PCA was used to encapsulate the perovskite NCs, the N atomic composition increased to 5.61% compared with 1.78% for the pristine NCs. Upon hydration of the PCA, the O atomic composition increased to 8.26% compared with 2.8% for the PCA-NCs (Table S1).

To construct a gas sensor OFET, a conductive polymer was integrated with the NCs as a carrier-transporting semiconductor. We fabricated blend films based on a conductive polymer, P3HT, with a mixture of the prepared perovskite nanoparticles (NCs, PCA-NCs, and PCA-w-NCs) (Fig. 3a). The perovskite NCs in the P3HT solution were spin-cast onto a Si wafer, resulting in NC-embedded conductive polymer thin films. The optical microscopy (OM) images of P3HT/NCs thin films show that the NCs are dispersed in the polymer matrix, forming 1–2 μm aggregates

(Fig. 3b). The nonpolar OA ligands attached to the perovskite NCs are highly compatible with chloroform; hence, the P3HT/NCs film exhibits a fine dispersion of NCs. On the contrary, the PCA-NCs blended in P3HT are more aggregated because of the polarity of the PCA polymer encapsulating the NCs, as evident in the TEM images (Fig. 1b). By comparison, the PCA-w-NCs are slightly less aggregated in P3HT than the PCA-NCs, forming a fine dispersion in the P3HT matrix, which might be attributable to smaller individual particles. To further investigate this matter, we captured high-resolution SEM images of the perovskite aggregates in the P3HT blend films, as displayed in Figs. S1, S2 and S3. Despite apparent aggregation, individual nanocrystals seem to retain their size and shape within the tens of nanometers scale, and the aggregates exhibit porous surface morphologies. We speculate that these aggregates can still effectively absorb NO₂ molecules at their surface. Furthermore, the primary focus of this study is to enhance gas sensing capabilities through the surface modification with zwitterionic polymers. We believe that this polymer modification at the surface amplifies NO₂ binding via intermolecular interaction, a process which is not significantly impeded by nanocrystal agglomerations.

The UV-Vis absorption spectra show that the crystallinity of the P3HT molecules improves with the addition of the NCs (Fig. 3c and S4). The UV-Vis absorption spectra of the P3HT films show characteristic absorption peaks at ~ 558 and ~ 606 nm due to intermolecular

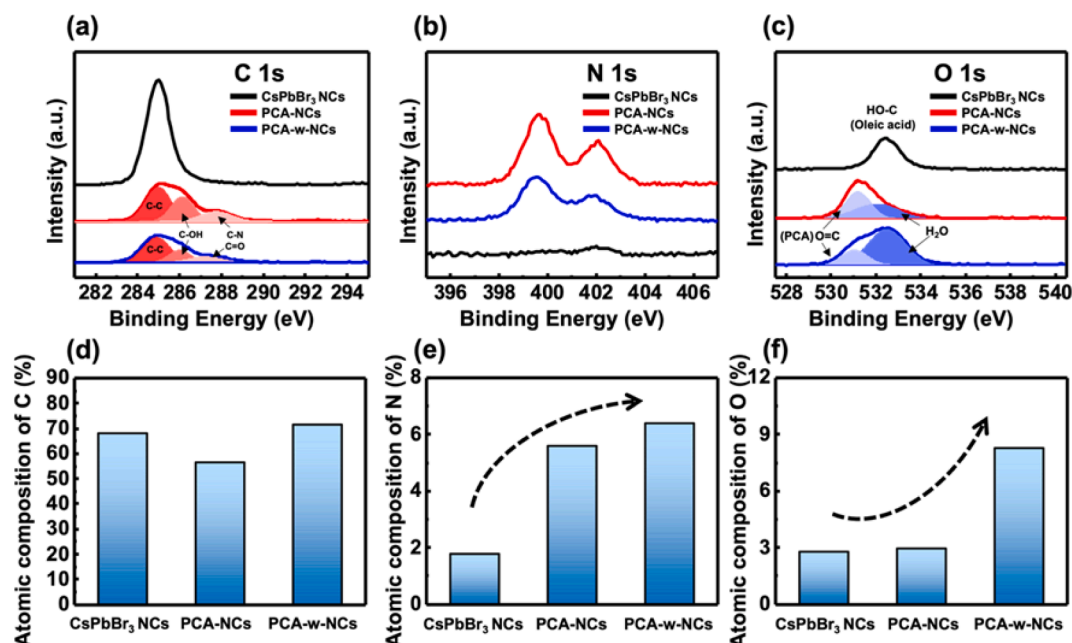


Fig. 2. XPS spectra of (a) C 1 s, (b) N 1 s, and (c) O 1 s elements in CsPbBr₃ NCs and the CsPbBr₃ NCs encapsulated with PCA and PCA-w. XPS atomic composition of (d) N and (e) O in the CsPbBr₃ NCs and the CsPbBr₃ NCs encapsulated with PCA and PCA-w.

interactions, which are assigned as the A_{0-0} and A_{0-1} absorption peaks, respectively; the spectra of the P3HT films can be compared on the basis of their A_{0-0}/A_{0-1} ratio. The ratio of the intensity of the A_{0-0} peak at 606 nm to that of the A_{0-1} peak at 558 nm is related to the degree of crystallinity of the P3HT films. The A_{0-0}/A_{0-1} peak ratio of thin films of P3HT mixed with NCs is greater than that of a pristine P3HT film (Fig. 3d). We speculate that the P3HT molecules exhibit strong self-assembly because of demixing between the polymer and the NCs. We also confirmed that the A_{0-0}/A_{0-1} peak ratio increases as the relative amount of NCs in the P3HT increases (Fig. S2–S4). However, the thicknesses of the blended thin films are roughly the same, in the range 80–90 nm. This increase in crystallinity is also observed in the films of P3HT/PCA-NCs and P3HT/PCA-w-NCs.

We fabricated bottom-gated P3HT field-effect transistors (FETs) to characterize the charge transport properties and gas-sensing behavior of the P3HT/NCs films (Fig. 4a) [41]. The transfer curves indicate characteristic p-type FET properties (Fig. 4b). The pristine P3HT device exhibits an on/off ratio of 8.5×10^2 and a field-effect mobility of $6 \times 10^{-4} \text{ cm}^2 \text{ V}^{-1} \text{ s}^{-1}$ (Fig. 4c). With the inclusion of NCs (P3HT/NCs), charge transport becomes more efficient, resulting in an increase in the field-effect mobility to $8 \times 10^{-3} \text{ cm}^2 \text{ V}^{-1} \text{ s}^{-1}$. This result is attributed not only to the increase in P3HT crystallinity but also to the charge doping effect from p-doped perovskite NCs. The P3HT/PCA-NCs device exhibits an increase in field-effect mobility to $3 \times 10^{-3} \text{ cm}^2 \text{ V}^{-1} \text{ s}^{-1}$ compared with that of the pristine P3HT device but is slightly lower than that of the P3HT/NCs device due to the insulating property of the PCA polymer. In addition, even in the case of the device based on hydrated PCA (P3HT/PCA-w-NCs), the charge transport is not substantially deteriorated compared with the P3HT/PCA-NCs device. The threshold voltage became positive when the P3HT was mixed with NCs, which is attributed to the accumulation of Br^- ions at the gate dielectric interface [42]. The charge transport associated with the migration of halide ions from the perovskite surface has been reported to be $\sim 0.4 \text{ eV}$, which can be increased by the gate bias. Interestingly, the P3HT/PCA-NCs and P3HT/PCA-w-NCs devices do not exhibit a threshold voltage shift as large as that of the P3HT/NCs device because of the effective passivation of the PCA polymer.

The gas-sensing performance of the FETs was characterized under exposure to NO_2 gas at the concentration of 10 ppm (Fig. 4d–f). We

examined the weight ratio of perovskite NCs in the P3HT blends to identify the optimal balance for FET mobilities and gas sensing performance. Irrespective of the type of NCs, the P3HT/perovskite blends exhibited their maximum responsivity with approximately 30 wt% of perovskite addition in the P3HT film (Fig. S5, S6, and S7). When the NC content was 50 wt%, the FET mobility of the devices decreased substantially, which also led to a decrease in responsivity because of the aggregation of the NCs (Fig. 4d and S3). To investigate the responsivity of the gas sensors, we repeatedly exposed the blended films to NO_2 (10 ppm) for 20 s and then purged the system with air for 200 s. The source-drain current (I_D) was measured at a V_G of -20 V and a V_D of -20 V , revealing an increase in current when the NO_2 gas was injected. The NO_2 sensing modulation of the I_D was improved with regard to the P3HT/NCs films compared with that of pristine P3HT (Fig. 4e). In addition, the introduction of PCA-NCs and PCA-w-NCs achieved more dramatic current modulation under NO_2 exposure. Importantly, the P3HT/PCA-w-NCs device showed the best performance among the investigated devices. The responsivity, response rate, and recovery rate were calculated from $\Delta I_D/I_0$, and $\Delta R/\Delta t$ and $\Delta R/\Delta t$ were obtained from the increasing and decreasing regions of the gas-response-time-current curves (Fig. 4f).

The gas responsivity of P3HT is greatly limited because of its small surface area and weak interaction with NO_2 gas; however, the P3HT with embedded NCs exhibited a greater surface area than the pristine P3HT and the NCs provided adequate adsorption sites for NO_2 molecules. In addition, the PCA-treated NCs substantially improved the gas responsivity because of the strong intermolecular interaction between the PCA and the NO_2 gas molecules. The PCA polymer interacts strongly with NO_2 molecules because of the amine groups in its side chain. In addition, the detachment of NO_2 from NCs was more efficient in the case of PCA-NCs, and the PCA-w-NCs exhibited the strongest NO_2 responsivity due to the specific chemical interaction between water molecules and NO_2 gas via hydrogen bonding, which is discussed further in the following section.

To investigate the gas sensitivity of the sensors, we compared the responses of OFET devices as a function of the concentration of various gases. First, we characterized the NO_2 gas-sensing performance of the P3HT FET manufactured with perovskite NCs (P3HT/NCs) (Fig. 5a and 5b) and compared it with the NO_2 -detecting performance of the P3HT/PCA-NCs and P3HT/PCA-w-NCs devices. By increasing the NO_2 gas

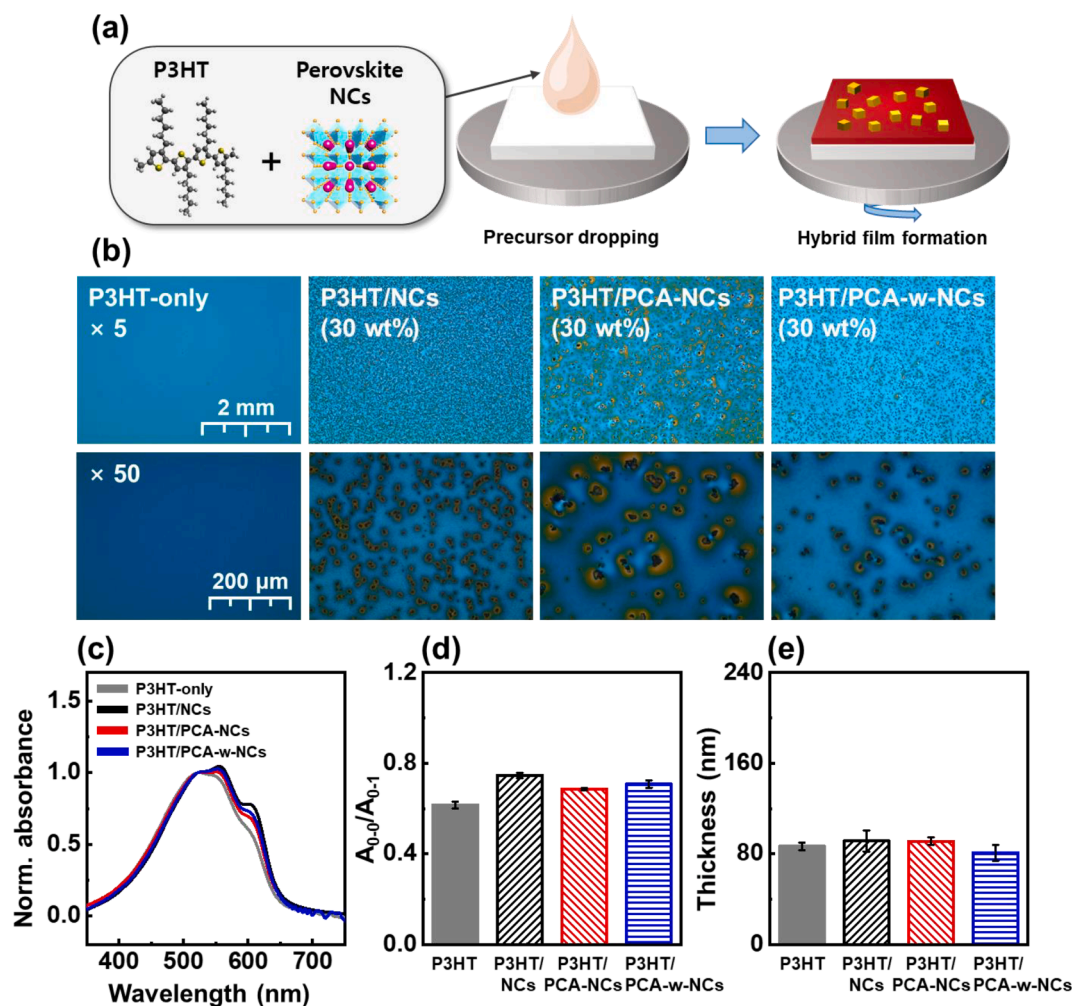


Fig. 3. Schematic of the fabrication method of P3HT/perovskite blend films. (b) Optical microscopy images of the P3HT-only, P3HT/NCs, P3HT/PCA-NCs, and P3HT/PCA-w-NCs films. (c) Absorption spectra of the P3HT-only, P3HT/NCs, P3HT/PCA-NCs, and P3HT/PCA-w-NCs films. (d) Peak ratio of $A_{0,0}$ to $A_{0,-1}$ and (e) film thickness of the P3HT-only, P3HT/NCs, P3HT/PCA-NCs, and P3HT/PCA-w-NCs films.

concentration from 10 to 100 ppm, we checked the dynamic response performance and calculated the sensitivity of the devices on the basis of the slope of the gas responsivity as a function of the analyte concentration. The P3HT/PCA-w-NCs devices showed the greatest sensitivity among the investigated devices. The perovskite NCs functionalized with hydrated PCA showed the highest gas-sensing performance with respect to sensitivity toward NO_2 , which is correlated with the intermolecular interaction between NO_2 gas molecules and water molecules on the PCA. The NO_2 molecules strongly interact with amine groups because of the electron-donating character of amines and water molecules [43,44].

Because gas selectivity is also an important parameter for gas sensors, we evaluated the sensor performance in the presence of SO_2 and CO_2 gases (Fig. 5c–f). When the analyte SO_2 gas was injected into the OFET gas sensors, the device with perovskite NCs exhibited a similar trend of increasing responsivity from P3HT to P3HT/NCs, P3HT/PCA-NCs, and P3HT/PCA-w-NCs. However, the degrees of responsivity and sensitivity of SO_2 adsorption were obviously lower than those of NO_2 adsorption. In addition, when the devices were exposed to the analyte CO_2 gas, those with perovskite NCs showed substantially reduced responsivity. Even with the addition of PCA-w-NCs, the CO_2 responsivity was one-half the SO_2 responsivity and one-fourth the NO_2 responsivity. These results are attributed to the difference in oxidizing power among NO_2 , SO_2 , and CO_2 leading to different intermolecular interactions, as reflected in the differences in responsivity among the OFET sensors. Among the devices with and without NCs, the P3HT/PCA-w-NCs device

showed the highest sensitivity and selectivity toward NO_2 at low concentrations, whereas it exhibited weaker responses for the other gases (SO_2 and CO_2) (Fig. 5g). We computed a theoretical detection limit based on methodologies outlined in previously published work and can be found in the [supplementary information](#) (Fig. S8) [45]. The lowest detectivity was compared in the PCA-w-NCs system, which demonstrated an NO_2 LOD of 0.000318 ppb, SO_2 LOD of 0.00112 ppb and CO_2 LODs of 0.00479 ppb (Fig. 5h). We expect the selective detection characteristics of the P3HT/PCA-w-NCs sensor to be beneficial for the detection of NO_2 at sub-ppb concentrations even under mixed-gas conditions.

To investigate the adsorption of gas molecules onto the perovskite NCs, we compared the binding energies of gas molecules using density functional theory (DFT) (Fig. 6a–c) [46–49]. On the basis of the PCA structure, the side chain, carboxybetaine acrylamide, was isolated to simplify the DFT calculations. The DFT modeling revealed that bonding of the PCA molecules to the perovskite surface via O atoms of the carboxylate moiety is the energetically favorable case. In the relaxed structure, the PCA molecule exhibits gas adsorption between two amine groups, which were used for structural relaxations to determine the optimal PCA–gas geometries and binding energies. The lowest-energy geometries had binding energies (E_b) of -4.43 eV (NO_2), -3.85 eV (SO_2), and -1.48 eV (CO_2) (Fig. 6b). The binding energies were calculated by the following equation [50,51],

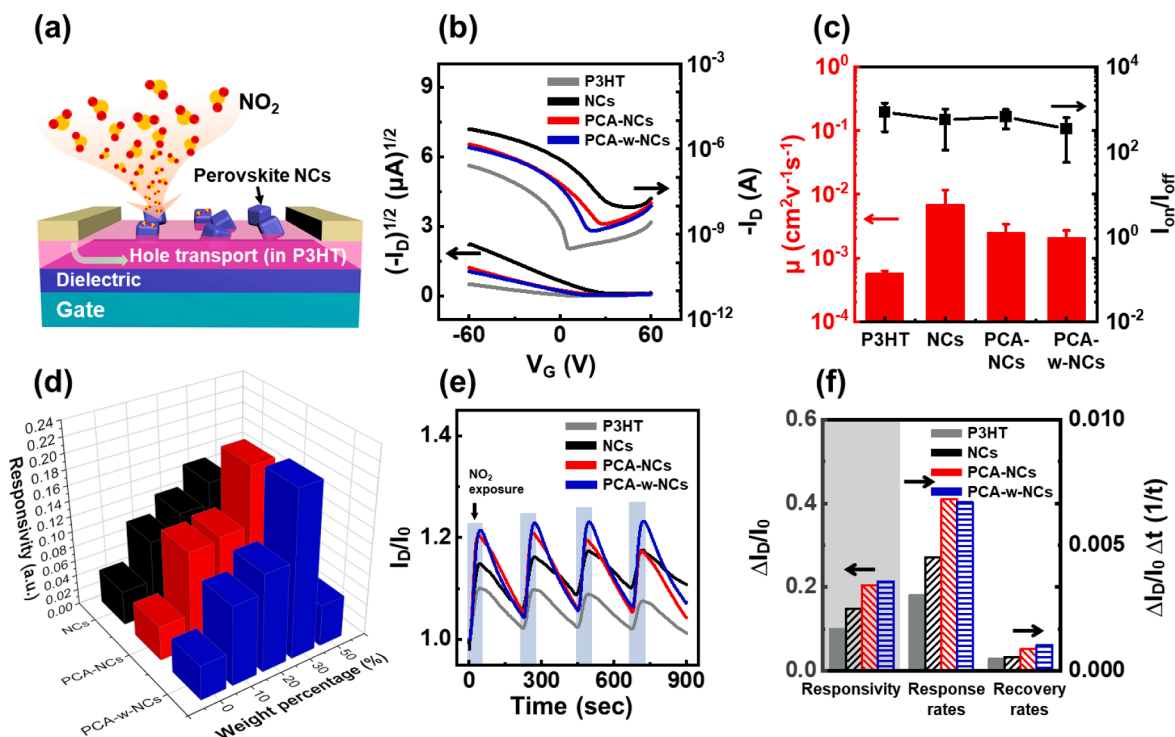


Fig. 4. (a) Field-effect transistor sensor structure of P3HT/NCs. (b) Charge transfer characteristics of the P3HT-only, P3HT/NCs, P3HT/PCA-NCs, and P3HT/PCA-w-NCs films. (c) Field-effect mobility and I_{on}/I_{off} ratio of the P3HT-only, P3HT/NCs, P3HT/PCA-NCs, and P3HT/PCA-w-NCs films. (d) Gas responsivity analysis of the P3HT-only, P3HT/NCs, P3HT/PCA-NCs, and P3HT/PCA-w-NCs films as a function of their NCs wt%. All sensing experiments were carried out at a gate voltage (V_G) of -20 V and a drain voltage (V_D) of -20 V. The blue rectangular region denotes a exposure time to NO_2 (20 s). (e) Source–drain current (I_D) vs. time (sec) curve based on OFET gas sensors repetitively exposed to NO_2 at 10 ppm. (f) Gas-sensing analysis of the responsivity, response rates, and recovery rates of the P3HT-only, P3HT/NCs, P3HT/PCA-NCs, and P3HT/PCA-w-NCs films. (For interpretation of the references to colour in this figure legend, the reader is referred to the web version of this article.)

$$E_b = E(\text{gas/PCA}) - E(\text{gas}) - E(\text{PCA})$$

where $E(\text{gas/PCA})$ is the total energy of a gas-adsorbed PCA molecule, $E(\text{gas})$ is the total energy of the gas molecule, and $E(\text{PCA})$ is the total energy of the PCA molecule. Because the amine group of the PCA polymer is likely to form a hydrogen bond with the O atom in NO_2 , the attachment of NO_2 to the polymer molecule is effectively promoted. The adsorbed NO_2 gas would oxidize the P3HT film, making the polymer p-doped and enhancing conductivity. The difference in the binding energies of NO_2 , SO_2 , and CO_2 supports the gas selectivity of the P3HT/PCA-NCs sensors. We further determined the binding energy of NO_2 on the hydrated PCA chain, which exhibited a maximum binding energy of -5.48 eV. We speculate that the hydrated PCA exhibits strong gas adsorption because of hydrogen bonding between the water in the hydrated PCA chain and NO_2 molecules. Such a strong chemical interaction of NO_2 gas molecules on water-saturated solid particles has been studied in atmospheric chemistry. Importantly, the surface-adsorbed water results in faster NO_2 uptake than the uptake observed for the naked nanoparticle surfaces.

One of the disadvantages of organic transistor-type gas sensors is poor device stability, which is closely related to deterioration by oxidative of the organic semiconductor[52–54]. A decrease in device stability leads to either a threshold-voltage shift or an off-current increase. In order to evaluate the stability of the organic transistors under ambient condition, transfer curves of the transistors were measured after they were exposed to ambient atmosphere at room temperature for a long time of storage (21 days). The organic p-type transistor exhibited threshold voltage (V_{th}) shift in the positive direction since it adsorbed water and oxygen, which is attributed to negative charges trapped by the adsorbed water and oxygen molecules at interface and the grain boundary. After 21 days storage under ambient atmosphere, the pristine

device showed an increase in its off-current and the largest positive shift of the threshold voltage compared to the other devices with perovskite NCs (Fig. 7a–d). The transfer curves show that the pristine device exhibited a continuous increase of V_{th} from 0 to 43 V after 21 days, whereas the NCs-P3HT device exhibited a smaller shift to +30 V. The PCA-NCs exhibited an even smaller shift of V_{th} to 25 V after 21 days under ambient conditions (Fig. 7e). We attribute this smaller V_{th} shift to the water and oxygen adsorbates on the perovskite NCs not penetrating through the P3HT layer at the bottom of the charge transport channels. More importantly, a simple vacuum process (30 mTorr for 10 min), which removed the captured oxygen and water molecules, restored the V_{th} to its original value. We calculated the recovery rate of the I_D after vacuum treatment using the following equation:

$$\text{recovery rate}(\%) = \frac{I_{re} - I_{21d}}{I_{0d} - I_{21d}} \times 100\%$$

where I_{0d} is the initial I_D value, I_{21d} is the I_D value of the aged device after the vacuum process. The pristine device exhibited only a 39% recovery rate, on the other hand, the devices blended with NCs showed recovery rates greater than 60%. Moreover, the device with the PCA-NCs showed an increase in recovery rate to 70%, and that with the PCA-w-NCs exhibited the highest recovery rate of greater than 80% (Fig. 7f). This high recovery indicates that the perovskite NCs adsorb oxygen and water molecules more intensively than the pristine P3HT and desorb the molecules more easily than the P3HT without NCs. These reversible adsorption and desorption behaviors of perovskite materials have been previously studied [55–57].

To characterize the air stability of P3HT films with NCs hybridization in the ambient atmosphere, we compared the C 1 s, O 1 s, and S 2p core-level peaks of each film before and after 21 days of atmospheric storage

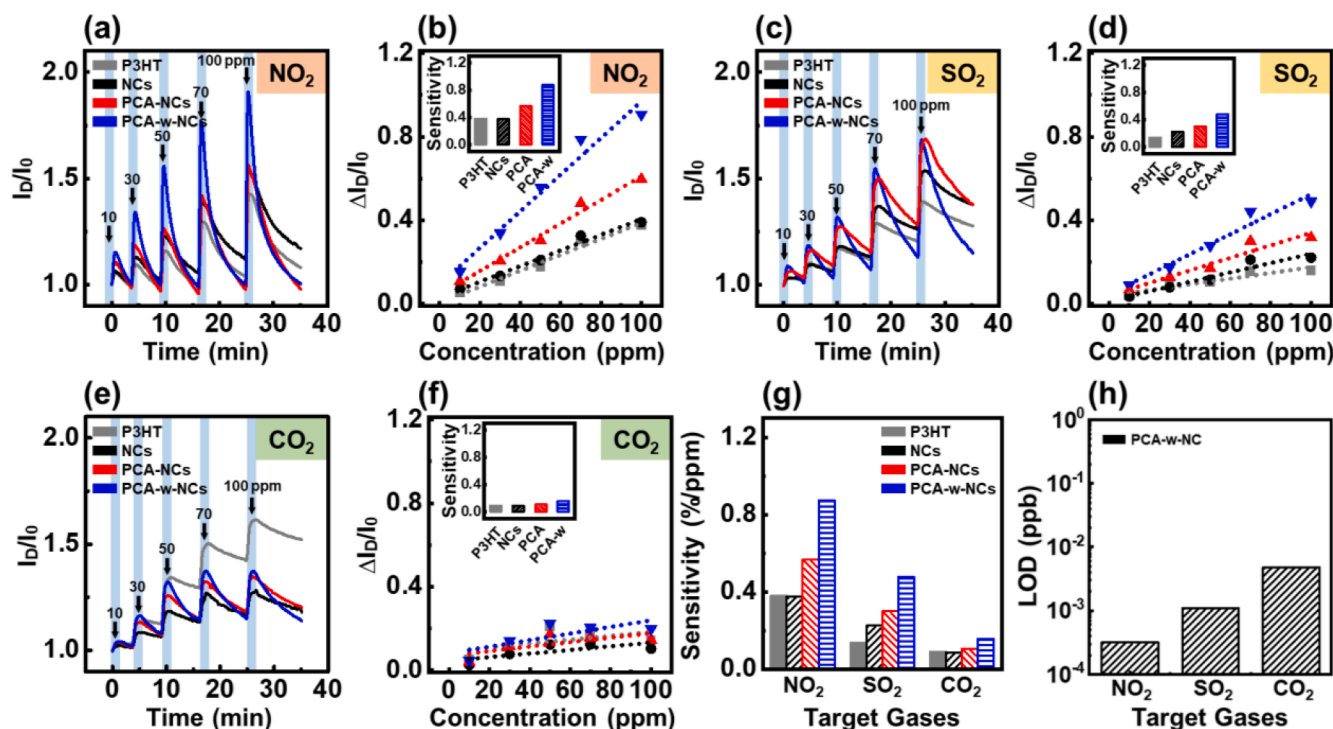


Fig. 5. (a) Source–drain current (I_D) vs. time curve of OFET gas sensors based on P3HT, P3HT/NCs, P3HT/PCA-NCs, and P3HT/PCA-w-NCs films when the sensors were exposed to various concentrations of NO_2 from 10 to 100 ppm. The blue rectangular region denotes a exposure time to NO_2 (20 s). (b) Linear fit shows the gas responsivity of the hybrid gas sensor devices as a function of the NO_2 concentration (the inset shows the calculated sensitivity determined from the slope of the fitted graphs). (c) Source–drain current I_D vs. time curve for OFET gas sensors exposed to various concentrations of SO_2 from 10 to 100 ppm. (d) Linear fit shows the gas responsivity of the blend sensor devices as a function of the SO_2 concentration. (e) Source–drain current I_D vs. time curve of OFET gas sensors exposed to various concentrations of CO_2 from 10 to 100 ppm. (f) Linear fit shows the gas responsivity of the blend sensor devices as a function of the CO_2 concentration. (g) Sensitivity of the gas-sensing FETs based on P3HT, P3HT/NCs, P3HT/PCA-NCs, and P3HT/PCA-w-NCs films, where the devices were exposed to NO_2 , SO_2 , and CO_2 gases. (h) Limit of detectivity (LOD) of the P3HT/PCA-w-NCs OFET gas sensor exposed to NO_2 , SO_2 , and CO_2 . (For interpretation of the references to colour in this figure legend, the reader is referred to the web version of this article.)

($T = \sim 20^\circ\text{C}$, relative humidity (RH) $\sim 30\%$) using XPS measurements. The C 1s core-level peaks of the pristine P3HT film, P3HT/NCs film, P3HT/PCA-NCs film, and P3HT/PCA-w-NCs film before and after 21 days were collected and deconvoluted using a Gaussian function to identify the carbon species: C–C (284.8 eV), C–O (286 eV), and C = O (287.5 eV) (Fig. 8a–d). In the case of the pristine P3HT film, the C1s spectrum shows a substantial increase in intensity of the C–O and C = O peaks after 21 days, which is direct proof of the oxidation of the P3HT chains (Fig. 8a). The spectrum of the blended P3HT/NCs film also shows a slight increase in intensity of the C–O peak at 286 eV after 21 days, but not as strong as the increase observed in the spectrum of the pristine P3HT film. However, in the spectra of the P3HT/PCA-NCs and P3HT/PCA-w-NCs blend films, the shape and intensities of the C 1s peaks are approximately the same even after 21 days of storage. These results are consistent with the results related to the device stability. We speculate that the strong interaction of PCA with water and oxygen protects the P3HT thin films from oxidation.

To further analyze the oxidative degradation of P3HT by water or oxygen molecules, we compared S core-level XPS spectra of the films before and after 21 days of storage under ambient conditions (Fig. 8e–h). The thiophene backbone of P3HT degrades with ring-opening under the chemical reaction with O_2 and OH^\bullet radicals formed by the interaction between water/oxygen molecules and the excited states of P3HT. The characteristic change of the S 2p peak as a result of P3HT degradation is a shift to a higher binding energy because of the electron removal and partial oxidation of P3HT. When the pristine P3HT thin film was exposed to ambient atmosphere for 21 days, the S 2p_{3/2} peak shifted by 0.12 eV with the higher binding energy. On the other hand, the XPS spectra of the P3HT/NCs composites didn't exhibit a corresponding peak

shift. These results demonstrate that the perovskite embedded in the P3HT matrix efficiently protected the polymer thin film from oxidative deterioration by adsorbing oxygen or water molecules before it was adsorbed by the polymer. This protective function of the perovskite NCs would ensure device stability as well as good gas sensitivity and selectivity in organic sensor applications.

To further confirm the stability, we performed XPS after storing the samples under the same conditions for a month. The binding energies measured matched those of the pristine perovskite sample, signifying minimal to no degradation. Particularly, Pb displays characteristic double peaks without any sub-peaks attributable to reduced metallic Pb. A minor shift to higher binding energies in Pb 4f and Br 3d suggests electronic interaction stemming from adsorbed oxygen and water molecules (Fig. S9). We also monitored the O 1s spectra over 21 days and found increases for all samples except those from PCA-NC and PCA-w-NCs. This observation suggests that gas molecules do not linger on the surface long enough to impact long-term stability (Fig. S10).

We also measured the electrical characteristics of the transistor-type gas sensor after storing it for 10 days under ambient conditions (RH $\sim 30\%$) (Fig. S11). The responsivity to NO_2 obtained from the sensor exposed to ambient conditions was slightly diminished compared to the non-exposed sensor, in the case of the pure P3HT device, even after vacuum treatment. The P3HT device did not fully recover, resulting in an elevated current level. However, the P3HT/PCA-NCs sensor restored its sensitivity to its original value. This clearly indicates that the P3HT/PCA-NCs sensor retains stable sensing functionality in ambient conditions.

The DFT results and device stability characteristics allow us to summarize the gas sensing mechanism of OFET devices employing

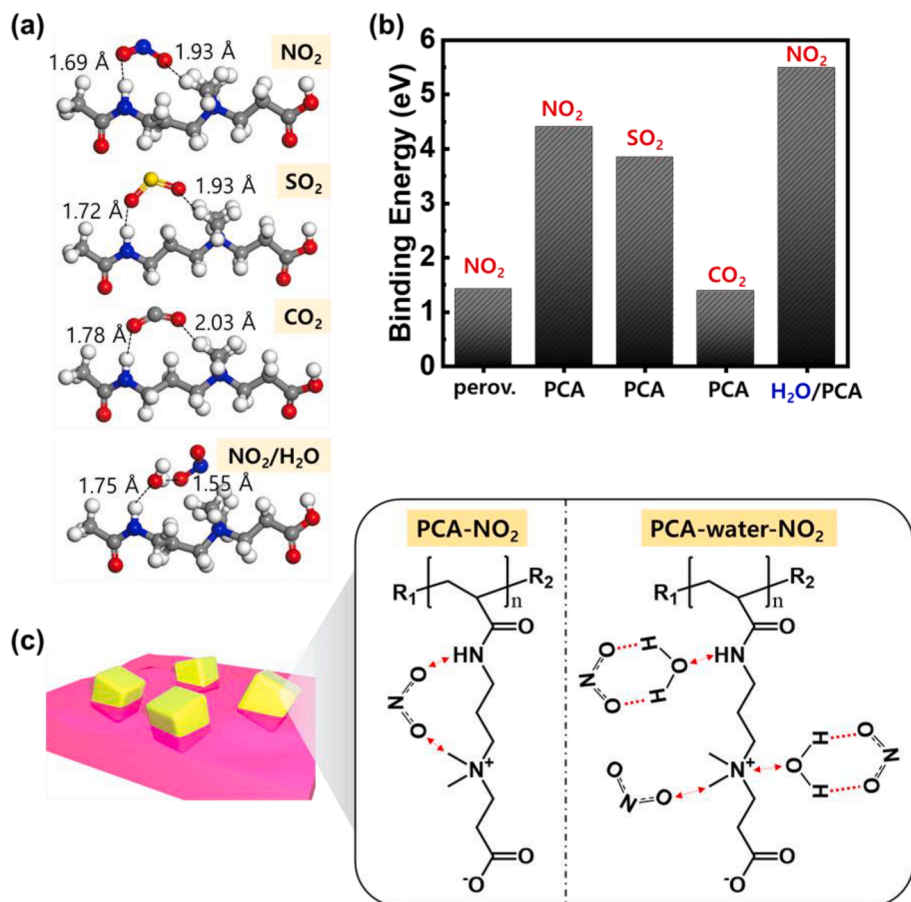


Fig. 6. (a) Adsorption configuration of NO₂ on PCA molecules. Red, gray, light-gray, blue, brown, purple, and light-blue spheres denote O, C, H, N, Br, Pb, and Cs atoms, respectively. Parts of the perovskite crystals have been removed for visualization purposes. (b) Binding energy of NO₂, SO₂, and CO₂ on PCA molecules, as calculated using DFT. (c) Schematic of the NO₂ sensing mechanism by PCA-w-NCs. With the introduction of NO₂, a PCA-gas interaction is established during the association process. (For interpretation of the references to colour in this figure legend, the reader is referred to the web version of this article.)

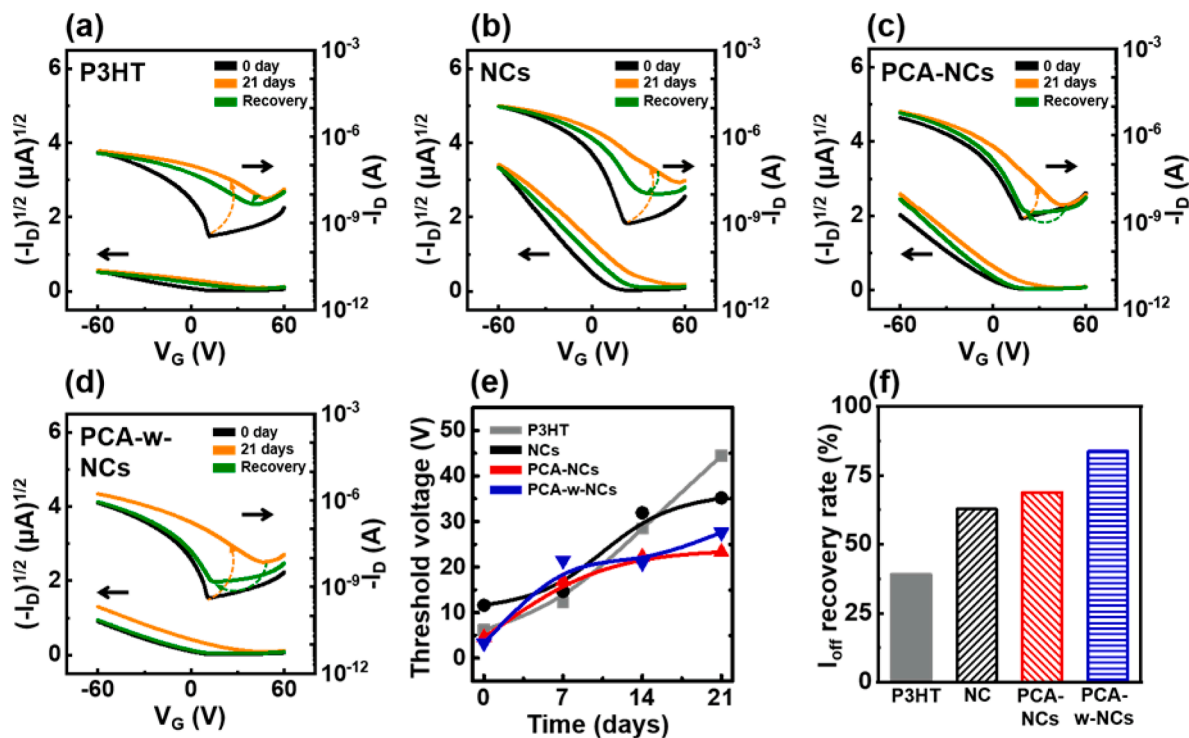


Fig. 7. Charge transfer characteristics of the OFET devices: (a) pristine, (b) P3HT/NCs, (c) P3HT/PCA-NCs, and (d) P3HT/PCA-w-NCs in the freshly prepared condition, after 21 days of storage under ambient conditions (average temperature of 20 ± 2 °C and average relative humidity of $\sim 30 \pm 10\%$), and after vacuum recovery. (e) Threshold voltage shifts as a function of storage time. (f) I_D recovery rate of a transistor fabricated using a P3HT/NCs blend film.

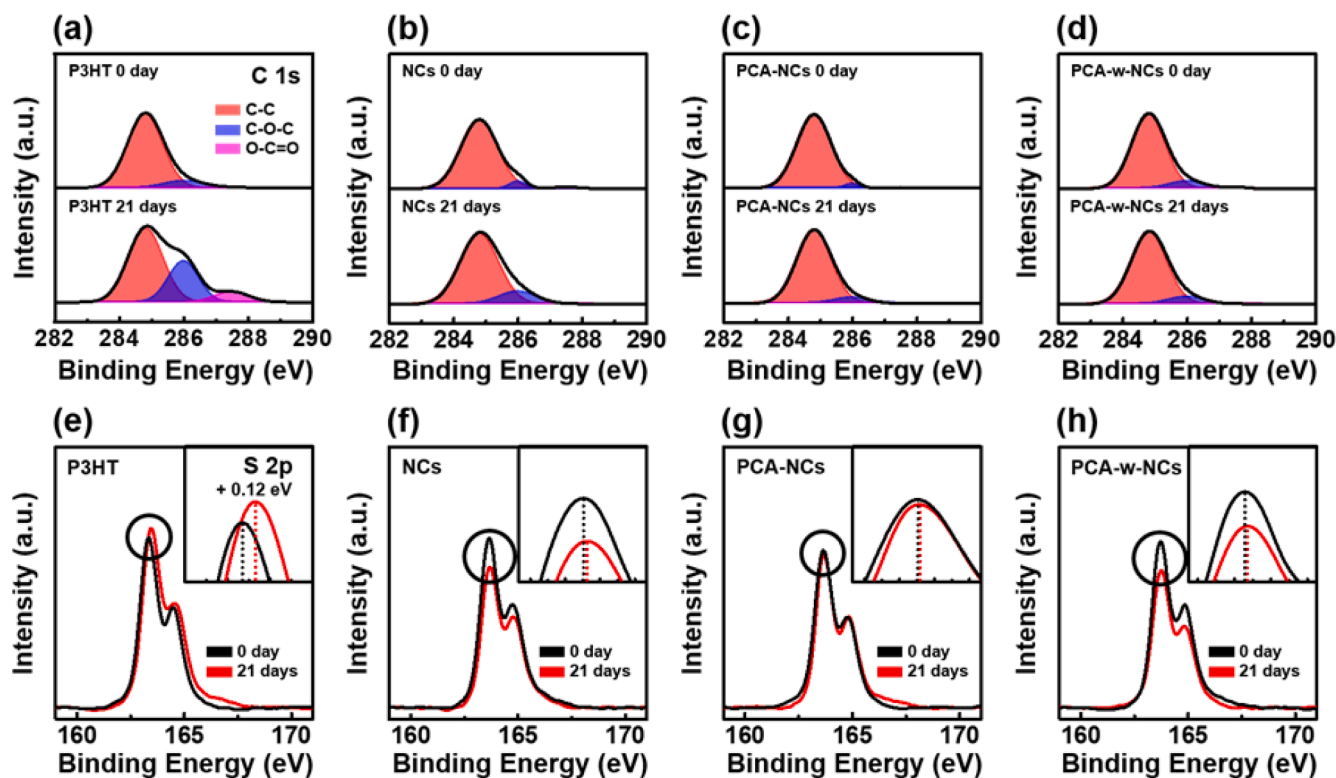


Fig. 8. XPS spectra of C 1s core-level peaks for (a) the pristine P3HT film, (b) P3HT/NCs(30 wt%) film, (c) P3HT/PCA-NCs(30 wt%) film, and (c) P3HT/PCA-w-NCs (30 wt%): film before and after 21 days of storage under ambient atmosphere. XPS spectra (e)–(h) show the O 1s core-level peaks and spectra (i)–(l) show the S 2p core-level peaks.

perovskite nanocrystals. The inherent ionic structure and high charge density of perovskite foster an efficient gas interaction at the nanocrystal surfaces, rendering them beneficial for gas sensor devices. In this study, we introduced perovskite nanocrystals into a P3HT OFET device with the aim of amplifying the gas sensitivity through charge modulation during exposure to NO_2 adsorption. However, repetitive exposure to highly oxidizing gas molecules such as NO_2 can cause degradation of both perovskite crystals and P3HT molecules. To mitigate this, we employed a PCA polymer encapsulation strategy for the perovskite nanocrystals. This not only shields the nanocrystals from degradation but also enhances gas interaction due to the ability of the PCA polymer to form hydrogen bonds with NO_2 gas molecules. We further augmented the NO_2 sensitivity by introducing water molecules into the PCA polymer, which, due to their high binding energies, results in an enhanced response. The NO_2 molecules adsorbed on the perovskite surfaces facilitate electron capture from the nanocrystals, which consequently affects the charge carrier density in the P3HT films. As a result, a dramatic reduction in current is observed, amplified by a strong p-doping effect stemming from the electron capture by the perovskite nanocrystals.

3. Conclusion

We have used perovskite NCs–conductive polymer composites to manufacture an OFET device for NO_2 gas sensor applications. The highly sensitive gas-capturing properties of the perovskite NCs enables them to function as gas adsorption sites in the polymer matrix, exhibiting superior and fast response to NO_2 with high sensitivity, a fast response rate, and a good recovery rate under ambient conditions. The PCA polymer used to encapsulate the NCs provides strong interaction between its functional amine group and NO_2 gas molecules, thereby improving the gas responsivity of the gas-sensing OFET device. Moreover, this novel perovskite–polymer hybrid sensor demonstrated

reproducible NO_2 sensing performance under ambient condition and selective sensing ability of NO_2 gas. These results indicate the application potential of organic–inorganic hybrid-based sensors. The results indicated here would provide a new approach to the development and design of gas sensors based on various material composites to achieve both superior sensitivity and selectivity.

4. Experimental section

4.1. Preparation and modification of the perovskite NCs

Metal halide perovskite (CsPbBr_3) NCs were prepared according to the modified hot-injection procedures described in the literature. In a three-necked flask, 0.325 g of Cs_2CO_3 was dissolved in 3.16 mL of OA, to which 1.84 mL of 1-octadecene (ODE) was added to adjust the concentration to 0.4 M. The solution was stirred at 110 °C for 30 min under a N_2 atmosphere. After the system was changed to a vacuum atmosphere, the mixture was stirred at 110 °C for 3 h. The system was then filled with N_2 , and the mixture was stored in a glove box.

In a three-necked flask, 0.138 g of PbBr_2 was dissolved in 10 mL of ODE and dehydrated at 120 °C for 30 min under vacuum. After the flask was filled with N_2 , 1 mL of dried OA and 1 mL of dried OAm were injected into the PbBr_2 solution and the resultant mixture was stirred at 120 °C for 20 min. After the temperature was increased to 160 °C, 0.25 mL of Cs-oleate for was injected. After 5 s, the three-necked flask was immersed into ice water. The CsPbBr_3 NCs were used after centrifugation with ethyl acetate and toluene. Two encapsulants, i.e., PCA (Polymer Sources, Canada) and PCA-w (hydrated polymer), were prepared by solution-based ligand exchange, as reported in the literature. The as-synthesized CsPbBr_3 NCs in a solution were mixed with the solution containing dissolved PCA to exchange the pre-attached OA/OAm ligands for the PCA polymer. The solutions were stirred at room temperature for 30 min to ensure complete ligand exchange, resulting in the

formation of PCA-NCs. The PCA-w-NCs were prepared by adding water (volume fraction of 5% relative to the volume of the PCA-NC solution).

5. Fabrication of OFETs and gas sensors based on the P3HT/perovskite thin films

The P3HT (Mw = 58 kDa, regioregularity = 96%, $2.0 \leq$ polydispersity index (PDI) ≤ 2.3) was purchased from Rieke Metals and was used as a p-type semiconducting material without additional purification. The P3HT solution was prepared to a concentration of 20 mg mL⁻¹ using chloroform, and the resultant solution was stirred at 50 °C for 1 h. Various amounts of the perovskite NCs (pristine CsPbBr₃, PCA-CsPbBr₃, and PCA-w-CsPbBr₃) were loaded in the same volume of chloroform and sonicated for 2 h at 50 °C. The prepared P3HT and perovskite solutions were combined, and stirred for 6 h at 50 °C using a hotplate/stirrer to prepare the P3HT/perovskite blend solution with a concentration of 10 mg mL⁻¹. A highly doped n-type Silicon wafer with a 3000 Å thick silicon dioxide (SiO₂) layer was sequentially sonicated with acetone and ethanol for 30 min in each solvent to remove organic contaminants. The Silicon wafer was then surface-modified with hexamethyldisilazane (HMDS) via a spin-casting method at 2500 rpm for 30 s. The P3HT/perovskite blend solution was spin-casted onto the HMDS-modified SiO₂/Si substrate at 2000 rpm for 60 s. Bottom-gate and top-contact (BGTC) type OFET devices based on the resultant perovskite/P3HT blended thin film were fabricated by thermally evaporating Au electrodes deposition. A square-patterned shadow mask with 100 μm channel lengths and 2000 μm channel widths was used to design the Au source and drain electrodes for OFET-based gas sensors. For UV-Vis absorption measurements, the P3HT/perovskite thin films were spin-casted onto cleaned glass substrates via the same process used to deposit films onto Silicon substrates.

6. Computational methodology

The optimization of gas-adsorption complexes and the calculation of binding energies, E_b , were performed by density functional theory (DFT) using the Dmol3 code. The LDA-PWC functional combined with DND basis set was applied in the calculations. The convergence threshold parameters for structure optimization were set as 1×10^{-5} H_a (energy), 0.002 H_a/Å (force), 0.005 Å (displacement), and the real-space orbital global cutoff was set as 3.3 Å. Betaineme structure was chosen to mimic PCA on the adsorption of NO₂. The binding energy of NO₂ was calculated by subtracting the sum of the energy of optimized gas-phase adsorbates and isolated PCA from the total energy of the optimized adsorbate – adsorbent complexes, which can be expressed by the following equations:

$$\text{In the case of dry PCA: } E_b = E_{\text{Total}} - (E_{\text{NO}_2} + E_{\text{PCA}})$$

$$\text{In the case of hydrated PCA: } E_b = E_{\text{Total}} - (E_{\text{NO}_2} + E_{\text{H}_2\text{O}} + E_{\text{PCA}})$$

6.1. Characterization

The crystal size and morphology of the NCs were characterized using a Cs corrected-field emission transmission electron microscope (JEM-ARM200F, JEOL, 200 kV) and Fourier transform infrared (FT-IR) spectroscopy was performed (Frontier, Perkin Elmer) using the Attenuated Total Reflection (ATR) method at the Future Energy Convergence Core Center (FECC). TEM and FTIR data were obtained at the Center for University-wide Research Facilities (CURF) of Jeonbuk National University. Powder XRD patterns of synthesized perovskites were determined using a X-ray diffractometer (MAX-2500, Rigaku, 40 kV) equipped with a Cu-Kα radiation source; samples were scanned the 2θ range 10–50° (scan rate = 4° min⁻¹). XPS was performed using a Nexsa XPS system (Thermo Fisher Scientific, UK) located at the Jeonju Center of the Korea Basic Science Institute (KBSI); all peaks were calibrated

against the C 1 s peak at a binding energy of 285 eV. The miscibility of perovskite nanocrystals in the P3HT thin films was inspected by OM (Olympus BX51) and SEM using the aforementioned scanning electron microscope. A UV-Vis spectrophotometer (Lambda 365, PerkinElmer) was used to measure the UV-Vis absorption spectra. The gas-sensing properties of the P3HT/perovskite thin films were analyzed at room temperature using a gas-sensor tester (Precision Sensor System, GASENTEST) and recorded with a Keithley 2636B semiconductor analyzer under an NO₂ concentration of 10 ppm with a V_G of –20 V and a V_D of –20 V. The NO₂ gas was supplied from a calibration gas cylinder containing NO₂ mixed with air. The dynamic sensing tests using NO₂, CO₂, and SO₂ at concentrations from 0 to 100 ppm were carried out under the same conditions, and the total flow rate was constant at 500 sccm (RH = 27.4%). The OFET performance was analyzed under ambient conditions (T_{avg} = ~20 °C, RH = ~30%) using a semiconductor analyzer (Keithley 4200-SCS). The humidity-exposed samples were measured after the samples were stored under dark and ambient conditions (RH of ~30%) for a specified period. The vacuum process was carried out by storing the humidity-exposed samples in a vacuum chamber at 30 mTorr and 400 L/min. The oxidative degradation of the P3HT backbones was analyzed by XPS (ULVAC-PHI, PHI 5000 Versa Probe II) using a monochromatic Al Kα X-ray source.

Declaration of Competing Interest

The authors declare that they have no known competing financial interests or personal relationships that could have appeared to influence the work reported in this paper.

Data availability

Data will be made available on request.

Acknowledgements

This work was supported by the National Research Foundation of Korea (NRF) grant funded by the Korea government (MSIT) (No. 2021R1C1C1012188) and (No. 2023R1A2C1005218).

Appendix A. Supplementary data

Supplementary data to this article can be found online at <https://doi.org/10.1016/j.cej.2023.145482>.

References

- [1] C. Zhang, P. Chen, W. Hu, Organic field-effect transistor-based gas sensors, *Chem. Soc. Rev.* 44 (8) (2015) 2087–2107.
- [2] S. Wang, Y. Kang, L. Wang, H. Zhang, Y. Wang, Y. Wang, Organic/inorganic hybrid sensors: A review, *Sens. Actuators B Chem.* 182 (2013) 467–481.
- [3] E. Oh, H.-Y. Choi, S.-H. Jung, S. Cho, J.-C. Kim, K.-H. Lee, S.-W. Kang, J. Kim, J.-Y. Yun, S.-H. Jeong, High-performance NO₂ gas sensor based on ZnO nanorod grown by ultrasonic irradiation, *Sens. Actuators B Chem.* 141 (1) (2009) 239–243.
- [4] T.L. Guidotti, The higher oxides of nitrogen: inhalation toxicology, *Environ. Res.* 15 (1978) 443–472.
- [5] A. Richters, K. Kuraitis, Inhalation of NO₂ and blood borne cancer cell spread to the lungs, *Arch. Environ. Health* 36 (1) (1981) 36–39.
- [6] F. Haghighi, Z. Talebpour, A. Sanati-Nezhad, Through the years with on-a-chip gas chromatography: a review, *Lab Chip* 15 (12) (2015) 2559–2575.
- [7] G. Korotcenkov, S.D. Han, J.R. Stetter, Review of Electrochemical Hydrogen Sensors, *Chem. Rev.* 109 (3) (2009) 1402–1433.
- [8] J. Hodgkinson, R.P. Tatam, Optical gas sensing: a review, *Meas. Sci. Technol.* 24 (1) (2013) 012004.
- [9] S. Hong, M. Wu, Y. Hong, Y. Jeong, G. Jung, W. Shin, J. Park, D. Kim, D. Jang, J.-H. Lee, FET-type gas sensors: A review, *Sens. Actuators B Chem.* 330 (2021) 129240.
- [10] F. Wang, Y. Dai, W. Wang, H. Lu, L. Qiu, Y. Ding, G. Zhang, Incorporation of Heteroatoms in Conjugated Polymers Backbone toward Air-Stable, High-Performance n-Channel Unencapsulated Polymer Transistors, *Chem. Mater.* 30 (15) (2018) 5451–5459.

- [11] B. Peng, S. Huang, Z. Zhou, P.K.L. Chan, Solution-Processed Monolayer Organic Crystals for High-Performance Field-Effect Transistors and Ultrasensitive Gas Sensors, *Adv. Funct. Mater.* 27 (29) (2017) 1700999.
- [12] G. Choi, K. Lee, S. Oh, J. Seo, E. Park, Y.D. Park, J. Lee, H.S. Lee, Electron-interfered field-effect transistors as a sensing platform for detecting a delicate surface chemical reaction, *J. Mater. Chem. C* 9 (26) (2021) 8179–8188.
- [13] B. Zhou, Z. Zhang, Y. Li, G. Han, Y. Peng, B.o. Wang, D. Zhang, J. Ma, C. Liu, Flexible, Robust, and Multifunctional Electromagnetic Interference Shielding Film with Alternating Cellulose Nanofiber and MXene Layers, *ACS Appl. Mater. Interfaces* 12 (4) (2020) 4895–4905.
- [14] J. Liang, Z. Song, S. Wang, X. Zhao, Y. Tong, H. Ren, S. Guo, Q. Tang, Y. Liu, Cobweb-like, Ultrathin Porous Polymer Films for Ultrasensitive NO(2) Detection, *ACS Appl. Mater. Interfaces* 12 (47) (2020) 52992–53002.
- [15] B. Kang, M. Jang, Y. Chung, H. Kim, S.K. Kwak, J.H. Oh, K. Cho, Enhancing 2D growth of organic semiconductor thin films with macroporous structures via a small-molecule heterointerface, *Nat. Commun.* 5 (2014) 4752.
- [16] Y. Jiang, W. Huang, X. Zhuang, Y. Tang, J. Yu, Thickness modulation on semiconductor towards high performance gas sensors based on organic thin film transistors, *Mater. Sci. Eng. B* 226 (2017) 107–113.
- [17] S. Wei, F. Tian, F. Ge, X. Wang, G. Zhang, H. Lu, J. Yin, Z. Wu, L. Qiu, Helical Nanofibrils of Block Copolymer for High-Performance Ammonia Sensors, *ACS Appl. Mater. Interfaces* 10 (26) (2018) 22504–22512.
- [18] V.V. Tran, G. Jeong, K.S. Kim, J. Kim, H.-R. Jung, B. Park, J.-J. Park, M. Chang, Facile Strategy for Modulating the Nanoporous Structure of Ultrathin π -Conjugated Polymer Films for High-Performance Gas Sensors, *ACS Sens.* 7 (1) (2022) 175–185.
- [19] J. Lu, D. Liu, J. Zhou, Y. Chu, Y. Chen, X. Wu, J. Huang, Porous Organic Field-Effect Transistors for Enhanced Chemical Sensing Performances, *Adv. Funct. Mater.* 27 (20) (2017) 1700018.
- [20] C. Liu, M. Wu, L. Gao, H. Liu, J. Yu, Nanoporous polymer films based on breath figure method for stretchable chemiresistive NO₂ gas sensors, *Sens. Actuators B* 371 (2022), 132540.
- [21] T. Mukhopadhyaya, J.S. Wagner, H. Fan, H.E. Katz, Design and Synthesis of Air-Stable p-Channel-Conjugated Polymers for High Signal-to-Drift Nitrogen Dioxide and Ammonia Sensing, *ACS Appl. Mater. Interfaces* 12 (19) (2020) 21974–21984.
- [22] F. Zhang, G.e. Qu, E. Mohammadi, J. Mei, Y. Diao, Solution-Processed Nanoporous Organic Semiconductor Thin Films: Toward Health and Environmental Monitoring of Volatile Markers, *Adv. Funct. Mater.* 27 (23) (2017) 1701117.
- [23] M. Khatib, T.-P. Huynh, J.J. Sun, T.T. Do, P. Sonar, F. Hinkel, K. Müllen, H. Haick, Organic Transistor Based on Cyclopentadithiophene-Benzothiadiazole Donor-Acceptor Copolymer for the Detection and Discrimination between Multiple Structural Isomers, *Adv. Funct. Mater.* 29 (9) (2019) 1808188.
- [24] B. Kwon, H. Bae, H. Lee, S. Kim, J. Hwang, H. Lim, J.H. Lee, K. Cho, J. Ye, S. Lee, W.H. Lee, Ultrasensitive N-Channel Graphene Gas Sensors by Nondestructive Molecular Doping, *ACS Nano* 16 (2) (2022) 2176–2187.
- [25] J. Hong, H.-J. Kwon, N. Kim, H. Ye, Y. Baek, C.E. Park, G.O. Choe, T.K. An, J. Kim, S.H. Kim, Solution-Processed Flexible Gas Barrier Films for Organic Field-Effect Transistors, *Macromol. Res.* 28 (8) (2020) 782–788.
- [26] E.H. Kwon, M. Kim, C.Y. Lee, M. Kim, Y.D. Park, Metal-Organic-Framework-Decorated Carbon Nanofibers with Enhanced Gas Sensitivity When Incorporated into an Organic Semiconductor-Based Gas Sensor, *ACS Appl. Mater. Interfaces* 14 (8) (2022) 10637–10647.
- [27] Q. Dong, Y. Fang, Y. Shao, P. Mulligan, J. Qiu, L. Cao, J. Huang, Solar cells. Electron-hole diffusion lengths > 175 μ m in solution-grown CH₃NH₃PbI₃ single crystals, *Science* 347 (2015) 967–970.
- [28] B. Gebremichael, G. Alemu, G. Tessema Mola, Conductivity of CH₃NH₃PbI₃ thin film perovskite stored in ambient atmosphere, *Phys. B Condens. Matter* 514 (2017) 85–88.
- [29] V.G.V. Dutt, S. Akhil, N. Mishra, Enhancement of photoluminescence and the stability of CsPbX₃ (X = Cl, Br, and I) perovskite nanocrystals with phthalimide passivation, *Nanoscale* 13 (34) (2021) 14442–14449.
- [30] Y. Zhao, K. Zhu, Organic-inorganic hybrid lead halide perovskites for optoelectronic and electronic applications, *Chem. Soc. Rev.* 45 (3) (2016) 655–689.
- [31] W. Jiao, J. He, L. Zhang, Synthesis and high ammonia gas sensitivity of (CH₃NH₃)PbBr₃-xI_x perovskite thin film at room temperature, *Sens. Actuators B Chem.* 309 (2020) 127786.
- [32] M.-Y. Zhu, L.-X. Zhang, J. Yin, J.-J. Chen, L.-J. Bie, B.D. Fahlman, Physisorption induced p-xylene gas-sensing performance of (C₄H₉NH₃)₂PbI₄ layered perovskite, *Sens. Actuators B Chem.* 282 (2019) 659–664.
- [33] E. Gagaoudakis, A. Panagiotopoulos, T. Maksudov, M. Moschogiannaki, D. Katerinopoulou, G. Kakavelakis, G. Kiriakidis, V. Binas, E. Kymakis, K. Petridis, Self-powered, flexible and room temperature operated solution processed hybrid metal halide p-type sensing element for efficient hydrogen detection, *J. Phys. Mater.* 3 (1) (2020) 014010.
- [34] C. Lu, M.W. Wright, X. Ma, H. Li, D.S. Itanze, J.A. Carter, C.A. Hewitt, G.L. Donati, D.L. Carroll, P.M. Lundin, S.M. Geyer, Cesium Oleate Precursor Preparation for Lead Halide Perovskite Nanocrystal Synthesis: The Influence of Excess Oleic Acid on Achieving Solubility, Conversion, and Reproducibility, *Chem. Mater.* 31 (2018) 62–67.
- [35] L. Protesescu, S. Yakunin, M.I. Bodnarchuk, F. Krieg, R. Caputo, C.H. Hendon, R. X. Yang, A. Walsh, M.V. Kovalenko, Nanocrystals of Cesium Lead Halide Perovskites (CsPbX₃, X = Cl, Br, and I): Novel Optoelectronic Materials Showing Bright Emission with Wide Color Gamut, *Nano Lett.* 15 (2015) 3692–3696.
- [36] M.C. Brennan, M. Kuno, S. Rouvimov, Crystal Structure of Individual CsPbBr₃ Perovskite Nanocubes, *Inorg. Chem.* 58 (2) (2019) 1555–1560.
- [37] M. Biondi, M.-J. Choi, O. Ouellette, S.-W. Baek, P. Todorović, B. Sun, S. Lee, M. Wei, P. Li, A.R. Kirmani, L.K. Sagar, L.J. Richter, S. Hoogland, Z.-H. Lu, F. P. García de Arquer, E.H. Sargent, A Chemically Orthogonal Hole Transport Layer for Efficient Colloidal Quantum Dot Solar Cells, *Adv. Mater.* 32 (17) (2020) e1906199.
- [38] J. Hong, B. Hou, J. Lim, S. Pak, B.S. Kim, Y. Cho, J. Lee, Y.W. Lee, P. Giraud, S. Lee, J.B. Park, S.M. Morris, H.J. Snaith, J.I. Sohn, S. Cha, J.M. Kim, Enhanced charge carrier transport properties in colloidal quantum dot solar cells via organic and inorganic hybrid surface passivation, *J. Mater. Chem. A Mater.* 4 (48) (2016) 18769–18775.
- [39] X. Guo, C. McCleese, W. Gao, M. Wang, L. Sang, C. Burda, Investigation of moisture stability and PL characteristics of terpineol-passivated organic-inorganic hybrid perovskite, *Mater. Renewable Sustainable Energy* 5 (4) (2016).
- [40] Y. Dong, X. Tang, Z. Zhang, J. Song, T. Niu, D. Shan, H. Zeng, Perovskite Nanocrystal Fluorescence-Linked Immunosorbent Assay Methodology for Sensitive Point-of-Care Biological Test, *Matter* 3 (1) (2020) 273–286.
- [41] A. Fujita, Y. Matsumoto, M. Takeuchi, H. Ryuto, G.H. Takaoka, Growth behavior of gold nanoparticles synthesized in unsaturated fatty acids by vacuum evaporation methods, *PCCP* 18 (7) (2016) 5464–5470.
- [42] N. Kaur, M. Singh, E. Comini, One-Dimensional Nanostructured Oxide Chemoresistive Sensors, *Langmuir* 36 (23) (2020) 6326–6344.
- [43] K. Ren, L. Huang, S. Yue, S. Lu, K. Liu, M. Azam, Z. Wang, Z. Wei, S. Qu, Z. Wang, Turning a disadvantage into an advantage: synthesizing high-quality organometallic halide perovskite nanosheet arrays for humidity sensors, *J. Mater. Chem. C* 5 (2017) 2504–2508.
- [44] B. Levasseur, A.M. Ebrahim, T.J. Bandosz, Interactions of NO₂ with amine-functionalized SBA-15: effects of synthesis route, *Langmuir* 28 (2012) 5703–5714.
- [45] J. Szanyi, J.H. Kwak, C.H.F. Peden, The Effect of Water on the Adsorption of NO₂ in Na– and Ba–Y, FAU Zeolites: A Combined FTIR and TPD Investigation, *J. Phys. Chem. B* 108 (2004) 3746–3753.
- [46] J. Li, Y. Lu, Q.i. Ye, M. Cinke, J. Han, M. Meyyappan, Carbon nanotube sensors for gas and organic vapor detection, *Nano Lett.* 3 (7) (2003) 929–933.
- [47] S. ten Brinck, I. Infante, Surface Termination, Morphology, and Bright Photoluminescence of Cesium Lead Halide Perovskite Nanocrystals, *ACS Energy Lett.* 1 (6) (2016) 1266–1272.
- [48] R. Pascazio, J. Zito, I. Infante, An Overview of Computational Studies on Colloidal Semiconductor Nanocrystals, *Chimia (Aarau)* 75 (2021) 427–434.
- [49] E. Mosconi, A. Amat, M.K. Nazeeruddin, M. Grätzel, F. De Angelis, First-Principles Modeling of Mixed Halide Organometal Perovskites for Photovoltaic Applications, *J. Phys. Chem. C* 117 (27) (2013) 13902–13913.
- [50] V. Rofati, E. Mosconi, A. Listorti, S. Colella, G. Gigli, F. De Angelis, Stark effect in perovskite/TiO₂ solar cells: evidence of local interfacial order, *Nano Lett.* 14 (2014) 2168–2174.
- [51] W. Zhang, H. Liu, X. Qi, Y. Yu, Y. Zhou, Y.u. Xia, J. Cui, Y. Shi, R. Chen, H.-L. Wang, Oxalate Pushes Efficiency of CsPb_{0.7}Sn_{0.3}Br₂ Based All-Inorganic Perovskite Solar Cells to over 14%, *Adv. Sci.* 9 (11) (2022) 2106054.
- [52] L. Hu, Q. Zhao, S. Huang, J. Zheng, X. Guan, R. Patterson, J. Kim, L. Shi, C.-H. Lin, Q. Lei, D. Chu, W. Tao, S. Cheong, R.D. Tilley, A.W.Y. Ho-Baillie, J.M. Luther, J. Yuan, T. Wu, Flexible and efficient perovskite quantum dot solar cells via hybrid interfacial architecture, *Nat. Commun.* 12 (2021).
- [53] X. Chen, Z. Wang, J. Qi, Y. Hu, Y. Huang, S. Sun, Y. Sun, W. Gong, L. Luo, L. Zhang, H. Du, X. Hu, C. Han, J. Li, D. Ji, L. Li, W. Hu, Balancing the film strain of organic semiconductors for ultrastable organic transistors with a five-year lifetime, *Nat. Commun.* 13 (2022) 1480.
- [54] T. Kubo, R. Hausermann, J. Tsurumi, J. Soeda, Y. Okada, Y. Yamashita, N. Akamatsu, A. Shishido, C. Mitsui, T. Okamoto, S. Yanagisawa, H. Matsui, J. Takeya, Suppressing molecular vibrations in organic semiconductors by inducing strain, *Nat. Commun.* 7 (2016) 11156.
- [55] Z. Lin, T. Kerle, T.P. Russell, E. Schäffer, U. Steiner, Electric Field Induced Dewetting at Polymer/Polymer Interfaces, *Macromol.* 35 (16) (2002) 6255–6262.
- [56] C. Bao, J. Yang, W. Zhu, X. Zhou, H. Gao, F. Li, G. Fu, T. Yu, Z. Zou, A resistance change effect in perovskite CH₃NH₃PbI₃ films induced by ammonia, *Chem. Commun.* 51 (84) (2015) 15426–15429.
- [57] H. Lee, D. Lee, H. Jin, D. Baek, M.K. Kim, J. Cha, S.K. Kim, M. Kim, Correction: Optical humidity sensors based on lead-free Cu-based perovskite nanomaterials, *Nanoscale Adv.* 4 (2022) 5189.